arXiv:cond-mat/0006128v3 [cond-mat.mtrl-sci] 26 Jun 2000

Influence of defects on the critical behaviour at the 105 K structural phase transition of $SrTiO_3$: II. The sharp component

H. Hünnefeld, T. Niemöller and J. R. Schneider
Hamburger Synchrotronstrahlungslabor HASYLAB at Deutsches Elektronen-Synchrotron DESY, Notkestr. 85, D-22603 Hamburg, Germany

U. Rütt
Argonne National Laboratory
9700 S. Cass Avenue, Argonne, IL 60439, USA

S. Rodewald, J. Fleig
Max-Planck-Institut für Festkörperforschung
Heisenbergstr. 1, D-70569 Stuttgart, Germany

G. Shirane
Department of Physics, Brookhaven National Laboratory
Upton, New York 11973, USA
(June 7, 2000)

The depth dependence of the crystallographic parameters mosaicity, lattice parameter variation and integrated reflectivity and of the critical scattering above the 105 K structural phase transition of $SrTiO_3$ have been studied in five different single crystals by means of high resolution triple-crystal diffractometry using $100 - 120$ keV synchrotron radiation. Depth-dependent impedance measurements indicate that the presence of oxygen vacancies is not responsible for the two-length scale phenomenon. It is found that the sharp component occurs only in surface near regions of highly perfect single crystals and is coupled to an exponential inrease of the crystallographic quantities. The second length scale is absent at a surface where the strain fields are able to relax by a macroscopic bending of the lattice planes. The sharp component is also strongly suppressed in crystals of relatively large mosaicity. The combination of long range strain fields in highly perfect samples and the vicinity of the surface seem to be necessary conditions for the observation of the sharp component. The critical exponents for the second length scale are in satisfying agreement with scaling laws if the intensity of the critical scattering is assumed to be proportional to the square of the Lorentzian susceptibility and not, as usual in the current convention, to a Lorentzian-squared susceptibility. The critical exponents of the broad component are independent of the appearance of the sharp component.

I. INTRODUCTION

According to modern theories of phase transitions based on the concept of scaling, the properties of the fluctuations associated with continuous phase transitions close to the critical temperature T_c are determined by a single length scale which varies with temperature. In contrast high resolution X-ray diffraction studies of structural phase transitions in perovskites revealed the existence of a second length scale in the critical fluctuations above T_c which had not been observed in earlier neutron scattering experiments. Later this effect has also been found in magnetic systems. The two length scale problem was discussed by Cowley [1]. The effect was first observed at the cubic-to-tetragonal second-order phase transition in $SrTiO_3$ at $T_c \approx 105\,\mathrm{K}$ and the temperature dependence of the two components has been studied by McMorrow et al. [2] usind 11 keV synchrotron radiation. Shirane et al. [3] showed that this sharp component is different from the central peak discovered by Riste et al. [4] in a study of the soft phonon mode. It has been shown that the sharp component originates from a volume element close to ($\approx 100\,\mu$m) the surface of the samples [5–7] and is related to the quality of the respective surfaces [5,8]. However, the nature of the defects responsible for the sharp component is not clear, e.g. Wang et al. [9] suggested the existence of edge dislocations close to the surface as to be responsible for the occurrence of the second length scale.

In this paper we present a systematic investigation of the critical scattering in different samples, differing by the respective growth technique, the amount of oxygen vacancies and the crystallographic quality. Using a beam of high energetic photons of $100 - 120\,\mathrm{keV}$ and $\sim 10\,\mu$m in height surface effects could be separated from bulk behaviour. The effect of the defects on the critical behaviour in the bulk of the samples has already been discussed in [10], hereafter referred to as paper I. In order to clarify the nature of the sharp component and the influence of defects on the occurrence of the second length scale the depth dependence of the crystallographic parameters mosaicity, lattice parameter variation and integrated reflectivity has been analysed and compared to the depth dependence of the critical behaviour.

After the description of the experimental setup of the diffraction experiments in section II, the characterisation of the different samples is reported in detail in section III. The measurements of the critical behaviour require a detailed determination of the critical temperatures [section IV]. The experimental results for the critical exponents are summarised in section V. Finally, the results are discussed in section VI. As an appendix mathematical details with regard to the resolution function are given in section A.

II. EXPERIMENTAL SETUP

The diffraction experiments have been performed with triple crystal diffractometers at the beamlines BW5 and PETRA2 at HASYLAB in Hamburg, using high energetic photons ($E \geq 100\,\mathrm{keV}$). The details of the experimental stations are described in [11] and [12–14], respectively. Due to the high photon energy of the incident beam, the photons penetrate through the crystal, i.e. all measurements have been performed in Laue-geometry. The critical scattering has been observed at the (511)/2-superlattice reflection position. Annealed silicon single crystals reflecting from (311) lattice planes were used as monochromator and analyser. The instrumental resolution in the scattering plane has been determined at the position of the superlattice reflection a few degrees below the transition temperature, examples are shown in figure 1. It results to $\Delta q_x = 1\times10^{-3}$Å^{-1} ($\Delta q_x$=1.5-3$\times10^{-3}$Å^{-1}) at PETRA2 (BW5) in the longitudinal direction [fig. 1a] and 1.6×10^{-4}Å$^{-1} \leq \Delta q_y \leq 2\times10^{-3}$Å^{-1} in the transverse direction [fig. 1b], depending on the mosaicity of the respective sample. Perpendicular to the scattering plane the resolution (HWHM) was of the order of $\Delta q_z = 1\times10^{-1}$Å^{-1}. A detailed description of the deconvolution of the experimental data is described in the appendix. The crystallographic perfection has been characterised at the (511) main reflection, with monochromator and analyser crystals using (624) reflections of perfect silicon. The difference in lattice spacing between sample and monochromator/analyser is $\sim 3.6\%$. Due to this almost dispersion-free setup the instrumental resolution is improved both in the longitudinal direction ($\Delta q_x = 1.2\times10^{-4}$Å^{-1}) and in the transverse direction ($\Delta q_y = 1.0\times10^{-5}$Å^{-1}).

In addition to the high **q**-space resolution also high real space resolution could be achieved with sufficient count ratio realising a narrow cross-section of the incident beam by means of a micro-slit and taking advantage of the high incident photon flux generated by the respective insertion devices at the beamlines. The spot size was reduced to a minimum height of $10\,\mu$m and a width of 2 mm. The surface of the sample was arranged parallel to the beam profile, the experimental procedure for the alignment of the micro-slit is given in [7]. By vertical translation of the sample the scattering volume can be moved to well-defined positions in the sample [see figure 2]. Due to the special geometry of the samples (the (511) reciprocal lattice vector is almost parallel to the investigated surface) it is possible to study the depth dependence of crystallographic quantities like strain and mosaicity with a spatial resolution of $\sim 10\,\mu$m. In the following, the depth $0\,\mu$m corresponds to the situation, where the complete beam just penetrates the sample. Consequently, at a depth of $-10\,\mu$m the beam is just passing by the sample. These positions are identified by

accurately measuring the dependence of the transmitted intensity as a function of the vertical position of the beam in the sample.

III. SAMPLES

The influence of defects on the critical behaviour of $SrTiO_3$ has been studied in various samples, differing in growth technique and heat treatments, which has been reported in paper I. In this paper we concentrate on the results for two highly perfect single crystals, namely sample I, which has been grown by the top-seeded method [15] more than two decades ago, and sample II, grown by the flux-grown technique [16]. Additionally, a series of Verneuil-grown samples has been investigated, an overview can be found in table I, details with regard to the sample preparation are given in paper I.

Searching for the origin of the sharp component, which occurs essentially close to the surface of the samples I [7] and II, first the depth dependence of strain, mosaicity and integrated reflecting power of these samples has been measured. As discussed in paper I, the existence of point defects, in this case oxygen vacancies, changes the values of the critical exponents if the mean distance of the defects is smaller than the correlation length of the critical fluctuations. Therefore the depth dependent concentration of the two-fold negatively charged oxygen vacancies has been investigated using impedance spectroscopy [17]: As described in [19] microelectrodes of different diameters can be used to analyse the depth dependence of the conductivity. Using gold microelectrodes ($15-220\,\mu$m) the conductivity measured at $\sim 200°$C could be shown to be depth-independent in the top $500\,\mu$mof both samples I and II. Oxygen vacancies considerably contribute to the overall conductivity at these temperatures and the conductivity data can be transferred into oxygen vacancy concentration values [18]. It can therefore be concluded that the vacancy concentration is depth-independent as well. Consequently, the sharp component, which has been observed in sample I up to a depth of $100\,\mu$m [7], is not related to a gradient in the oxygen vacancy concentration. This is an important finding because the sharp component has only been found in the crystallographically rather perfect samples with relatively high concentrations of oxygen vacancies and not in the less perfect Verneuil crystals with much lower oxygen vacancy concentrations. In the Verneuil-grown samples the vacancy concentration of the bulk has been determined from conventional impedance measurements of the isolating as-grown and oxidised samples using the vacancy mobility [18] and by Hall-resistivity measurements for the almost metallic reduced sample. The results are summarised in table I.

The main focus of this paper is on sample I, where a direct correlation between strain, lattice parameter variation and the occurrence of the sharp component in the critical scattering was observed in the surface near region up to a depth of $100\,\mu$m, also using triple crystal diffractometry at energies of ~ 120 keV [7]. Based on these results a $560\,\mu$m thick slice has been cut from the same sample. Figure 2 shows a schematical drawing of the sample before and after cutting. On the left hand side the original sample is plotted. The capital letter A marks the region investigated in [7]. The rectangular spots visualise the beam cross-sections on the sample, however, the dimensions are not to scale. The sample size is about $1\,\mathrm{cm}^3$, whereas the cross-section of the beam was $10\,\mu\mathrm{m}\times 2\,\mathrm{mm}$. The cut was performed parallel to the surface in a depth of about one millimeter, using a diamond saw. The residual plate has a thickness of $\sim 560\,\mu$m, the material loss due to sawing and careful polishing of the two cut faces resulted to about 1 mm. In figure 2 also the notation for the following discussion is defined. Region B is the surface near region of the upper face of the residual plate, which has not been polished or changed in any way compared to the former measurements in region A in [7]. The region at the lower surface of the plate is labeled C. This surface corresponds to a depth of $560\,\mu$m with respect to the original sample surface. The region on top of the residual block is labeled D, originally this part of the crystal was in a depth of ~ 1.5 mm from the surface of the original block, i.e. it represented the bulk of the original sample where no sharp component was observed. The two surfaces C and D had been subject to the identical polishing treatment. Region E represents the bulk of the block. The depth dependent impedance measurements described above have been performed in region A, at the original sample.

The depth dependence of the integrated intensity, the mosaicity and the variation of the lattice parameter has been measured at the (511) main reflection around the phase transition temperature of ~ 100 K for the different surfaces B–D and in the bulk E of sample I. In figure 3 the gain in the integrated intensity of the (511) reflection in region D compared to the intensity I_{bulk} in the bulk (region E) is plotted as a function of the distance to the surface of the residual block. The straight line is an exponential function $(I - I_{bulk}) \propto \exp(-z/\zeta)$ fitted to the data. No temperature dependence can be observed, the mean $1/e$-length results to $\zeta = 26(1)\,\mu$m. The increase of intensity can be understood qualitatively on the basis of dynamical diffraction theory [20,21]. The bulk mosaicity of the sample is determined by transverse scans in reciprocal space, it results to a FWHM of $\Delta\omega_2 = 0.5$". The width of the (511) reflection of an absolutely perfect $SrTiO_3$-crystal at 100 keV is $FWHM_{dyn} = 0.086$", i.e. the mosaicity is about a factor of 6 larger than the dynamical width. This broadening is not an effect of the instrumental resolution but represents the intrinsic mosaic spread of the sample, which is still much smaller than in the other samples, especially

the Verneuil grown samples with mosaic spreads of $30 - 100$". The integrated reflectivity in the bulk expected for a perfect crystal can be calculated for negligible absorption using dynamical theory. One obtains $I_{dyn}/I_0 = 3.2 \times 10^{-7}$, where I_0 is the transmitted intensity behind the sample in the anguar range where no Bragg scattering occurs, i.e. the effect of absorption is eliminated. In the bulk (region E) the measured integrated reflectivity I/I_0 was about 7.7 times larger than the theoretical value for a perfect crystal. This is consistent with the increase in the mosaic spread. However, using the kinematical scattering theory, the expected integrated reflectivity of the 12 mm thick sample should be $I_{kin}/I_0 = 7.0 \times 10^{-5} \approx 220 \cdot I_{dyn}/I_0$. Thus the diffraction mechanism in the bulk of this sample is close to the expectations for a perfect crystal, which has been shown before by means of γ-ray diffraction experiments [22]. Close to the surface the mosaic spread of the sample increases [Fig. 4], and therefore the scattering process has to be described more and more by kinematical scattering theory, which explains the increase of the integrated reflectivity, shown in figure 3. The widths (HWHM) of the transverse scans ($\Delta\omega_2$), corresponding to the mosaicity, and the widths (HWHM) of the longitudinal scans ($\Delta\omega_3$), corresponding to the variation of the lattice parameter ($\Delta d/d = \frac{1}{2} \cdot \cot\theta_B \cdot \Delta\omega_3$, θ_B is the Bragg-angle) follow the same exponential depth dependence as the integrated intensity shown in figure 3, the results are plotted fig. 4.

The identical characterisation of the crystallographic properties was carried out for the platelet (regions B and C). Figure 5 shows the data of the integrated intensity in the platelet and simultaneously the width (HWHM) of the longitudinal scans, i.e. the lattice parameter variation, at a temperature of 120 K. On the left side of the figure, which corresponds to region B, the behaviour is identical to that in region D, shown in figure 3. Within the errorbars, the $1/e$-length ($\zeta = 25(1)\,\mu$m) is the same. But, surprisingly, the other surface of the plate (region C) does not show any effect, neither for the integrated intensity, nor for the widths of longitudinal and transverse scans. In fact, the integrated reflectivity is identical to the bulk value in region E, whereas the variation of the lattice parameter, $\Delta d/d$ is slightly enhanced compared to the bulk value. These results are also summarised in figure 4.

The intrinsic mosaicity of the platelet could not be determined within these measurements because the platelet turned out to be bent. Due to the relatively large width of the beam spot, the signal results from an overlap of different regions in the bent sample, which enhances the width of the transverse scans. Consequently, the width of the transverse scans at a given spot is a measure of the bending radius of the plate and not a measure of the intrinsic mosaicity. A more accurate determination of the bending radius was achieved by using a narrow cross-section of the beam, e.g. $50 \times 50\mu\text{m}^2$, and measuring the shift of the position of a main reflection depending on the position in real space on the plate, which was oriented perpendicular to the beam. Using this technique, a real-space picture of the plate can be reconstructed from the data [Fig. 6]. The bending of the lattice planes is almost spherical, the bending radius results to ~ 14 m. In this figure, region C corresponds to the upper, concave side, i.e. the lower, convex side corresponds to region B. Using an optical microscope it could be seen that not only the lattice planes are bent but the platelet itself is bent macroscopically. It should be mentioned that the bending has been observed not directly after the polishing process but after the first low temperature measurements, i.e. after the platelet had undergone the structural phase transition. Thus it is not clear if the bending process took place directly after the polishing process or some weeks later after cooling through the transition.

Supplementary to the depth dependent measurements with 100 keV photons, the surfaces B–D have been investigated in Bragg geometry with a photon energy of 20 keV on a triple-axis diffractometer at the HASYLAB beamline D4 [23]. The absorption length at this energy was determined to $\mu^{-1} \sim 55\,\mu$m, i.e. the relevant contribution to the Bragg peaks results from the surface near region of some ten microns thickness. In figure 7 the scattering profiles of the (200) Bragg reflection are shown for the three surfaces B,C and D both in linear scale and in logarithmic scale (inset). At the surface of the residual block (region D) a difference between the center of the surface and the edge region of the surface was found. It can be seen, that regions B and D (center) show much broader Bragg peaks than region C and the edge of the residual block (D edge). Additionally, the integrated intensity of the respective scans is shown in the legend. Consistent with the observations described above, the values are increased at surfaces B ($I = 427$) and D ($I = 321$), compared to surface C ($I = 210$). However, interestingly the edge region of the residual block shows a similar behaviour as the cut surface of the plate (region C).

The characterisation of the crystallographic quantities in sample I can be summarised as follows: The residual floatzone grown block consists of an almost perfect bulk (region E) surrounded by a layer (region D) of increased mosaicity and increased lattice parameter variations. Both mosaicity and lattice parameter variation increase exponentially with an 1/e-length of $26(1)\,\mu$m approaching the surface. This behaviour is identical to the depth dependence of the experimental data from the original sample before the cut (region A), presented in [7], and supports the interpretations of the earlier γ-ray diffraction experiments on the same sample in [22]. However, the region D close to the surface of the residual block, which has been inside the almost perfect bulk of the sample before the cut, strongly changed its crystallographic properties after cutting and polishing the surface. On the other hand, the cut surface of the residual plate, i.e. region C shows no effects in the mosaicity or the integrated reflectivity. The values are the same as those of the bulk (region E), only a slightly enhanced value of the lattice parameter variations is observed. In spite of the identical treatment of surfaces C and D, large differences are observed. The behaviour of the untreated

surface of the plate, region B, remains unchanged compared to the earlier measurements at region A.

The only explanation for the observed difference in the behaviour of regions C and D can be given by the fact that the plate became bent after the cut. Assuming that the original sample included long range strain fields inside the bulk, possibly introduced by the growth process, a relaxation of these strain fields is not possible in the residual block because of its dimensions and the high crystallographic perfection. In region D, close to the surface of the residual block, these strain fields lead to an increased mosaicity and increased lattice parameter variations in the center of the surface, but not in the edge regions of the surface of the residual block because here the strain fields are able to relax. Similarly the relaxation of the strain fields is observed in the platelet. The existing strain gradient in the platelet, experimentally determined at region A in [7], is able to relax by bending the whole thin sample. Hence, in region C no dislocations like in region D are observed, the crystallographic parameters remain unchanged compared to the bulk behaviour. However, the other surface, region B, still is full of dislocations and thus also does not change its general behaviour. Due to the large dimensions of the crystal, this bending process of course is not possible at the surface of the residual block, in region D.

Similar measurements have been carried out on sample II, it can be seen that the surface of sample II qualitatively shows the same behaviour like the regions A, B and D of sample I. The mosaicity of sample II is about one order of magnitude larger than that of sample I, but it is still much better than the mosaic spreads of 30-100" of the Verneuil-grown crystals. The depth dependence of the crystallographic parameters of the Verneuil-grown crystals has not been investigated.

IV. CRITICAL TEMPERATURES

Essential for the discussion of critical behaviour and the determination of critical exponents is the accurate measurement of the critical temperature. Following the procedure of Riste et al. [4], the temperature dependence of the integrated intensity of a superlattice reflection has been measured both below and above the phase transition. The scattered intensity at this position is proportional to the square of the order parameter, $I \propto \langle\varphi\rangle^2 = \langle\varphi_0 + \delta\varphi\rangle^2$. Unfortunately, just below T_c both the critical fluctuations $\langle\varphi^2\rangle$ and the static part $\langle\varphi_0\rangle^2$ contribute to the signal. Above T_c the critical fluctuations give rise to a tail in the temperature dependence of the order parameter [figure 9]. As described in paper I, we have neglected the contribution of static order parameter clusters, which do also exist above T_c. Using the Landau approximation, the susceptibilitiy at $T_c - \Delta T$ is a factor of 2 smaller than the susceptibility at $T_c + \Delta T$ [see e.g. [24]]. This relation is used to substract the contribution of the fluctuations below T_c as described in [4]. The temperature dependence of the residual data I' can be fitted with a power law:

$$I' \propto \langle\varphi_0\rangle^2 \propto \left(\frac{T - T_c}{T_c}\right)^{2\beta} \tag{1}$$

In order to maximise the compatibility of the critical temperatures T_c, the critical exponent β was fixed to $\beta = 0.34$ [4]. Slight changes in β were allowed to determine the error bars of the critical temperatures. The results for the critical temperature in the bulk of the various samples are summarised in table I. The value $T_c = 98.8(2)\,\mathrm{K}$ for sample I has been determined in the bulk of the original sample. Usually, in literature, the critical temperature of the structural phase transition in $SrTiO_3$ averages to about 105 K. This value is similar to the value for the two Verneuil samples with low oxygen vacancy concentrations. It has been shown earlier, that an increased amount of oxygen vacancies reduces the critical temperature [25,26], the reduced Verneuil sample nicely reproduces the results. However, the shift in the critical temperature for the two highly perfect samples I and II is much too large compared to the experimentally determined concentration of oxygen vacancies. The origin of this observation is not clear yet, perhaps the high degree of perfection of samples I and II is responsible for the low transition temperature. As pointed out by Zhong et al. [27], the existence of quantum fluctuations leads to a significant decrease of the critical temperature of about 20 K. It might be speculated that the quantum fluctuations show a stronger effect in the more perfect samples than in the worse Verneuil samples, which leads to an additional decrease of the phase transition temperature.

In analogy to the crystallographic characterisations described above, the depth dependence of the critical temperature has been investigated in detail in sample I. The results are plotted in figure 8. Both the transition temperatures before and after the cut are shown. As to be expected no changes in T_c are observed in region E, the bulk of the sample. In the original sample two features can be identified: Over a large range the critical temperature is decreasing and close to the surface, in region A, a slightly enhanced value for T_c is found. The latter observation is similar to the behaviour at the surface of the residual block, region D. There also a slight increase in the critical temperature is found very close to the surface ($\sim 20\,\mu$m). However, in the residual plate the general trend is unclear. $50\,\mu$mbelow the cut surface (region C) of the plate, T_c is identical to the bulk value (region E), but at both surfaces, regions B and C, the critical temperature decreases substantially. Comparing these observations with the results of the crystallographic

characterisation, it can be concluded that two different effects have to be distinguished. On one hand, the probably large amount of dislocations and other defects, which are not yet identified, in region A is responsible for the large difference in the transition temperatures found in the bulk and near the surface of the original block. On the other hand, it seems that the strain fields in its surface near region increase the transition temperatures slightly. This is observed in region A and region D, but not in region C, where the strain fields are absent. After the relaxation of the strain gradient in the plate, the critical temperature in region C is close to the bulk value (region E). In region B T_c strongly declines almost to the low value observed at the original surface (region A).

Another interesting result of the measurements is the behaviour of the tails of the order parameter above the critical temperatures. In order to compare the tails for the different samples, the integrated intensities of the superlattice reflection have been normalised to the respective scaling factor of the fitted power law, i.e. the extrapolated value at zero temperature. Also, the temperature is replaced by the reduced temperature $\tau = \frac{T-T_c}{T_c}$. Using this method, the effect of the stronger, more kinematical scattering at the surface [see section III] is cancelled out and all curves except one coincide below the transition temperature, as can be seen in figure 9. The additional information derived from this kind of presentation is the similarity of the temperature dependence of the tails above the critical temperatures. In the residual block [fig. 9a], all data points follow the same trend above T_c, i.e. the nature of the tails is not connected to the observed strain gradients at the surface. Moreover, the tails are identical in the residual block and in the residual plate [fig. 9b], only the old surface of the plate, region B, shows a significantly enhanced amount of scattering above T_c. Certainly, this has to be attributed to the large amount of dislocations and/or other defects in this region.

V. THE SHARP COMPONENT IN THE CRITICAL SCATTERING

The critical scattering has been observed at the position of the (511)/2 superlattice reflection in the samples I and II and at the position of the (531)/2 superlattice reflection in the Verneuil samples. In most cases, after deconvolution of the experimental resolution [see appendix A] the scattering profile could be fitted with a single Lorentzian distribution function and as a result the inverse correlation length κ_{Lor} and the susceptibility χ_{Lor} of the broad component in the critical scattering could be extracted. Plotting this as a function of temperature it is possible to deduce the values of the critical exponents ν_b and γ_b, which has been discussed in detail in paper I. In this paper, we want to focus on the sharp component, which has been observed only in samples I and II in surface near regions. In those cases the scattering profile had to be fitted with a sum of a Lorentzian and a Lorentzian-squared profile, i.e. two additional parameters, the inverse correlation length σ_{Lq} and the susceptibility χ_{Lq}, have to be taken into account (the peak-position of the two contributions turned out to be identical). A typical example of a measured scattering profile is shown in figure 10. The Lorentzian-squared part is much narrower than the Lorentzian contribution, which is the reason for calling it the sharp component.

At a temperature about 1 K above T_c the depth dependence of the critical scattering profile in the residual block of sample I is shown in figure 11. In the top 20 μm, corresponding to region D, the additional sharp component is clearly visible. In the inset, the same data are plotted over a wider angular range in logarithmic scale. This is to stress the observation that the broad component is independent of the location of the probed volume element in the sample. The scattering only differs in the central region, where the sharp component dominates. The temperature dependence of the inverse correlation length for the broad component was identical at all investigated positions in sample I after the cut. The values ν_b and γ_b for the critical exponents of the broad component in the different samples and for the various positions in the samples are summarised in table II. As discussed in paper I, the absolute values depend on the concentration of the oxygen vacancies. However, all values of the critical exponents related to the broad component can be explained in terms of the influence of order parameter clusters, the universal behaviour is not restricted. For the different positions in sample I the critical exponents for the broad component are almost identical, i.e. the occurrence of the sharp component as well as the increased mosaicity and lattice parameter variations do not affect the behaviour of the broad component. In table II also the validity of some scaling relations is checked (α, β, γ, ν and η are the well-known critical exponents, d is the dimensionality of the system, in this case $d = 3$).

$$\gamma = (2-\eta)\nu \tag{2}$$

$$2-\alpha = \gamma + 2\beta$$

$$2-\alpha = d\nu$$

$$\Rightarrow \beta = \frac{1}{2}(d\nu - \gamma) \tag{3}$$

The value of η is very small (~ 0.03) for $SrTiO_3$ [28], i.e. the ratio γ_b/ν_b should be close to 2. Especially the Verneuil-samples almost perfectly fulfill this condition, overall this scaling relation holds quite nicely in all cases.

Using relation (3), the obtained value of β might be compared with the results below T_c, where β was fixed to the value 0.34. In the surface near regions B and D this scaling relation seems to fail, but with respect to the large error bars the agreement is satisfying for most of the samples.

The dircet comparison between the three surfaces of the residual floatzone grown-sample, i.e. regions B, C and D is shown in figure 12. Apparently, the width of the sharp component in region B is much broader than the respective width in region D. Furthermore, almost no signal of the sharp component is visible in region C. The profiles for regions C and D are identical except for a narrow region in the center of the scan, which is due to the sharp component. In figure 13 the plots from which the critical exponents γ_s [fig. 13a] and ν_s [fig. 13b] have been determined are shown for the four positions where the sharp component was observed. Again, the old surface of the cut-off plate, region B, strongly differs from all other data sets. The resulting values for the critical exponents of the sharp component are listed in table III. The strong deviation of the behaviour in region B is obvious, the second length scale in the three other regions is described by similar critical exponents. Interestingly, the ratio γ_s/ν_s is noticeable larger than 2, more likely close to 4. The validity of scaling relations for the sharp component could be established, if the intensity of the sharp component is not proportional to the susceptibility but to the square of the susceptibility, as it is also the case e.g. for Huang-scattering [29]. The two functions

$$I_{Lq} = \frac{\chi_{Lq}}{\left(1+\left(\frac{\mathbf{q}}{\sigma_{Lq}}\right)^2\right)^2} = \hat{\chi}_{Lq}(\mathbf{q},T) \tag{4}$$

and

$$I_{Lq} = \left(\frac{\chi'_{Lq}}{1+\left(\frac{\mathbf{q}}{\sigma_{Lq}}\right)^2}\right)^2 = \hat{\chi'}^2_{Lor}(\mathbf{q},T) \tag{5}$$

only differ by the definition of the respective susceptibility. All critical exponents discussed so far have been derived using equation (4). However, assuming a Lorentzian distribution and using the latter definition, the susceptibility χ_{Lq} is replaced by $\chi'_{Lq} = \sqrt{\chi_{Lq}}$. As a result the value of the critical exponent is reduced by a factor of two, $\gamma'_s = \gamma_s/2$ and the ratio γ'_s/ν_s is close to two, fulfilling the scaling relation (2).

Concluding, the sharp component in the critical scattering in $SrTiO_3$ occurs in surface near regions (some ten microns) of highly perfect crystals, but not if long range strain fields are absent in this region. The temperature dependence of the correlation length and the susceptibility can be described with critical exponents, which do fulfill scaling relations if a definition of the scattering profile different from current convention is applied. The occurrence of the sharp component does not affect the critical behaviour of the broad component in any manner.

VI. DISCUSSION

We have investigated the critical scattering above the 105 K structural phase transition of $SrTiO_3$. The main focus is put on the dependence of the critical phenomena on the depth below the surface. In order to interpret the results concerning the critical scattering, the crystallographic perfection was analysed with high momentum- and real-space resolution especially in the regions close to the surfaces. Particularly we concentrated on the differences of several surfaces of a highly perfect sample.

As a result it is observed that one necessary condition for the existence of two length scales in the critical scattering is the vicinity (some ten microns) of the surface of a sample. Another necessary condition is the existence of strain fields in this region, experimentally demonstrated by the increase of lattice parameter variations and mosaicity close to the surface. However, in samples of lower quality, i.e. with strongly enhanced mosaic spreads the sharp component is suppressed significantly compared to that found in the highly perfect crystals. Possibly the long range order of the critical fluctuations is destroyed by the high amount of topological defects in samples of very high mosaicity.

Starting with the bulk of sample I, region E, no sharp component can be observed, because it is not a surface near region. In region D, both conditions are fulfilled. Both mosaicity and the variation of the lattice parameter, as well as the critical temperature, increase exponentially approaching the surface and the exisitence of long range strain fields at this surface seems reasonable. Simultaneously, also the intensity of the sharp component increases, while the broad component remains unaffected. Region C consists of an almost perfect crystal, where the strain fields were able to relax by bending of the lattice planes. Thus, no sharp component is observed and the critical temperature is close to the bulk value. On the other hand, region B, the "old" surface of the plate, still is full of dislocations and

probably other unspecified defects. Here, both conditions for the appearence of the sharp component are fulfilled, but different from the surface of the residual block, region D, a lot of dislocations exist at this surface stemming from the frequent use over more than twenty years in many experiments. Moreover, the bending of the lattice planes additionally deteriorated the crystallographic perfection, because unlike the other almost perfect surface no relaxation was possible at this surface. The development of long range correlations at this surface is suppressed or, at least, affected. The result is the large deviation in the values of the critical exponents for the sharp component in region B, compared to the earlier results on the same surface before the cut, called region A. The behaviour of sample II at the surface is very similar to the behaviour of sample I in region D. The surface of sample II was cut, polished and etched, as described in paper I. Afterwards in the surface near region mosaicity, lattice parameter variation and the intensity of the sharp component increased simultaneously. Compared to the two almost perfect samples the intensity of the sharp component in the Verneuil-grown samples III-V is suppressed by about three orders of magnitude, i.e. no evaluation of critical exponents for this component was possible. This is due to the large mosaicity, which suppresses the long range correlation comparable to the effect at the old surface of the plate (region B). Qualitatively, it has been shown before that at distorted surfaces the intensity of the sharp component is reduced [5,8].

In conclusion, long range strain fields in the vicinity of the surface seem to be responsible for the second length scale in the critical scattering of $SrTiO_3$. These long range strain fields can spread out much better in almost perfect crystals, dislocations and other topological defects reduce the strain fields and affect the critical exponents and eventually lead to complete suppression of the second length scale. Similar to the usual critical fluctuations, the temperature dependence of the long range correlations can be described with a set of critical exponents, also we presented indications for the validity of scaling laws. However, the distribution of defects in the surface near region is crucial for the formation of the sharp component and for the values of the critical exponents describing this phenomenon. This interpretation of the nature of the sharp component is consistent with the ideas of Cowley [1], who suggested that at the surface the coupling of strain fields to the order parameter might lead to free surface waves with a higher effective transition temperature than the bulk fluctuations. The sharp component is then attributed to the free surface fluctuations. Unfortunately, no quantitative calculations on the basis of this approach have been performed yet. Further theoretical work is needed for a full quantitative understanding of the nature of the second length scale in the critical scattering.

ACKNOWLEDGEMENTS

We would like to thank H.J. Scheel for making available the flux-grown $SrTiO_3$ crystal, S. Kapphan for preparing the Verneuil crystals and E. Courtens for stimulating remarks. Valuable comments from B. Kaufmann and F. Schwabl are gratefully approved. Support by US Department of Energy under contract No. DE-AC02-98CH10886 is acknowledged.

APPENDIX A: DECONVOLUTION OF THE RESOLUTION FUNCTION

In order to extract the correlation length and the susceptibility from the experimental data, first the experimental resolution function had to be determined. The deconvolution procedure is based on the paper by Hirota et al. [30]. In the scattering plane, the resolution function was determined experimentally at the position of the superstructure reflection a few degrees below the transition temperature [see fig. 1]. From these scans we extracted the widths in the longitudinal ($FWHM_x$) and in transvere ($FWHM_y$) directions and the shape of the respective scattering profiles. In most cases, the shape of the superstructure peak was a lorentzian-squared profile. The functional form of the resolution element was approximated by:

$$R(q_x, q_y) = \left(1 + \left(\frac{q_x}{\sigma_x}\right)^2 + \left(\frac{q_y}{\sigma_y}\right)^2\right)^{-2} \tag{A1}$$

$$\sigma_{x,y} = \frac{FWHM_{x,y}}{2\sqrt{\sqrt{2}-1}}$$

For the investigated samples this approximation is in very good agreement with the correct resolution function, the theoretical calculation is explained in detail in [31,32]. Perpendicular to the scattering plane, the resolution is determined by the opening of the vertical slits, substantially by the widths of the slits in front of the sample (S_{z1}) and in front of the detector (S_{z2}). These widths have to be transformed to the **q**-space using the distance L between sample and detector and the value of the wavevector **k**:

$$W_{zi} = |\mathbf{k}| \cdot \frac{S_{zi}}{L} \tag{A2}$$

The resolution element $R(q_z)$ is now given by the convolution of two rectangular profiles, which is a trapezoidal function, as shown in figure 14:

$$R(q_z) = \begin{cases} 0 & \forall & |q_z| \geq q_1 \\ \frac{|q_z|-q_1}{q_2-q_1} & \forall & q_2 < |q_z| < q_1 \\ 1 & \forall & |q_z| \leq q_2 \end{cases} \tag{A3}$$

$$q_1 = \frac{1}{2}(W_{z1} + W_{z2})$$

$$q_2 = \frac{1}{2}|W_{z1} - W_{z2}| \tag{A4}$$

For an incident intensity I_0 the scattered intensity $I(\mathbf{q})$ results to

$$\frac{I(\mathbf{q})}{I_0} = \int\int\int dq'_x dq'_y dq'_z R(q'_x, q'_y) \cdot R(q'_z) \cdot I_{crit}(\mathbf{q} - \mathbf{q}') \quad , \tag{A5}$$

where I_{crit} is the intrinsic profile of the critical scattering, typically a lorentzian distribution. As described above, in some cases the critical scattering can not only be described by a single lorentzian profile. We used an additional isotropic lorentziansquared function to fit the experimental data.

$$I_{crit} = I_{Lor} + I_{Lq} \tag{A6}$$

$$I_{Lor} = \frac{\chi_{Lor}}{1 + \sum_{i=x,y,z} \left(\frac{q_i - q_{i,0}}{\kappa_{Lor,i}}\right)^2} \tag{A7}$$

$$I_{Lq} = \frac{\chi_{Lq}}{\left(1 + \left(\frac{\mathbf{q}-\mathbf{q_0}}{\sigma_{Lq}}\right)^2\right)^2} \tag{A8}$$

According to [3], the lorentzian contribution shows an anisotropy , the inverse correlation lengths κ_{100} in (100)-directions are a factor of 1.8 smaller than the widths κ_{011} in (011)-directions. In our experiments the scattering geometry was such that $q_x \parallel (511)$, $q_y \parallel (\bar{1}50)$ and $q_z \parallel (\bar{5}\,\bar{1}\,26)$, i.e. all three directions are slightly tilted with respect to the main axes. For simplicity we assumed $\kappa_x \approx \kappa_y \approx \kappa_z \approx \kappa_{100} \equiv \kappa_{Lor}$, probably slightly underestimating the correct inverse correlation length.

The integration in q_z in equation (A5) was performed analytically. Using the symmetry of the resolution function, the integral reduces to

$$\int dq'_z R(q'_z) \cdot I_{crit}(\mathbf{q} - \mathbf{q}') = 2\int_0^{q_2} dq'_z I_{crit}(\mathbf{q} - \mathbf{q}') + 2\int_{q_2}^{q_1} dq'_z \frac{q'_z - q_1}{q_2 - q_1} \cdot I_{crit}(\mathbf{q} - \mathbf{q}') \tag{A9}$$

The integral consist of four parts, two addends for both the lorentzian I_{Lor}^{conv} and the lorentziansquared contribution I_{Lq}^{conv}. Now we define

$$b_L^2 = \kappa_{Lor}^2 + (q_x - q'_x)^2 + (q_y - q'_y)^2 \tag{A10}$$

$$b_{Lq}^2 = \sigma_{Lq}^2 + (q_x - q'_x)^2 + (q_y - q'_y)^2 \tag{A11}$$

and set $q_z = 0$, because we are only looking at the intensity in the scattering plane. The result for the lorentzian part can be written as

$$I_{Lor}^{conv} = \frac{\chi_{Lor}\kappa_{Lor}^2}{b_L} \cdot \left(2\arctan\left(\frac{q_2}{b_L}\right) + \frac{j_1 - j_2}{q_2 - q_1}\right) \tag{A12}$$

where

$$j_1 = b_L \cdot \ln(b_L^2 + q_1^2) - 2q_1 \arctan(q_1/b_L) \tag{A13}$$

$$j_2 = b_L \cdot \ln(b_L^2 + q_2^2) - 2q_1 \arctan(q_2/b_L) \quad . \tag{A14}$$

Equation (A12) can be simplified to:

$$I_{Lor}^{conv} = \frac{\chi_{Lor}\kappa_{Lor}^2}{q_2 - q_1} \cdot \left(\ln\left(\frac{b_L^2 + q_1^2}{b_L^2 + q_2^2}\right) - 2\frac{q_1}{b_L}\arctan\left(\frac{q_1}{b_L}\right) + 2\frac{q_2}{b_L}\arctan\left(\frac{q_2}{b_L}\right)\right) \tag{A15}$$

Similarly the integration of the lorentziansquared part yields:

$$\begin{aligned} I_{Lq}^{conv} &= \frac{\chi_{Lq}\sigma_{Lq}^4}{b_{Lq}^3(b_{Lq}^2 + q_2^2)} \cdot \Bigg(q_2 b_{Lq} + (q_2^2 + b_{Lq}^2) \cdot \arctan\left(\frac{q_2}{b_{Lq}}\right) \\ &+ b_{Lq}q_2^2 - q_1 b_{Lq} + q_1(b_{Lq}^2 + q_2^2) \cdot \left(\arctan\left(\frac{q_1}{b_{Lq}}\right) - \arctan\left(\frac{q_2}{b_{Lq}}\right)\right)\Bigg) \\ \Leftrightarrow I_{Lq}^{conv} &= \frac{\chi_{Lq}\sigma_{Lq}^4}{b_{Lq}^3(q_2 - q_1)} \cdot \left(q_2 \arctan\left(\frac{q_2}{b_{Lq}}\right) - q_1 \arctan\left(\frac{q_1}{b_{Lq}}\right)\right) \end{aligned} \tag{A16}$$

The remaining calculations,

$$\frac{I(q_x, q_y)}{I_0} = \int\int dq_x' dq_y' R(q_x', q_y') \cdot (I_{Lor}^{conv} + I_{Lq}^{conv}) \quad , \tag{A17}$$

have been evaluated numerically, using the approximation (A1) for the resolution element in the scattering plane, and were compared to experimental data $I(q_x = 0, q_y)$ for transverse scans or $I(q_x, q_y = 0)$ for longitudinal scans in every step of the fitting procedure.

In order to check the validity of the theoretical calcuations, two different values for the vertical resolution have been set up, without changing any parameter of the sample and its surrounding. By narrowing the detector slit the vertical resolution has been improved by a factor of 20. As shown in figure 15, the improvement of the resolution suppresses the intensity of the broad component much more than the intensity of the sharp component in the center of the scan. However, applying the fitting procedure described above the fitted values for the correlation lengths and the susceptibilities were independent of the resolution width. This observation we take as a verification of the calculations presented in this section.

[1] R. Cowley, Phys. Scr. T **66**, 24 (1996).
[2] D. McMorrow *et al.*, Solid State Commun. **76**, 443 (1990).
[3] G. Shirane, R. Cowley, M. Matsuda, and S. Shapiro, Phys. Rev. B **48**, 15595 (1993).
[4] T. Riste, E. Samuelsen, K. Otnes, and J. Feder, Solid State Commun. **9**, 1455 (1971).
[5] T. Thurston *et al.*, Phys. Rev. B **49**, 15730 (1994).
[6] H.-B. Neumann, U. Rütt, J. Schneider, and G. Shirane, Phys. Rev. B **52**, 3981 (1995).
[7] U. Rütt *et al.*, Europhys. Lett. **39**, 395 (1997).
[8] G. Watson *et al.*, Phys. Rev. B **53**, 686 (1996).
[9] S. Wang, Y. Zhu, and S. Shapiro, Phys. Rev. Lett. **80**, 2370 (1998).
[10] H. Hünnefeld *et al.*, Phys. Rev. B (2000), submitted.
[11] R. Bouchard *et al.*, J. Synchrotron Rad. **5**, 90 (1998).
[12] HASYLAB, Annual report **I**, 139 (1995).
[13] HASYLAB, Annual report **I**, 58 (1996).
[14] C. Oeser, S. Keitel, H. Hünnefeld, and J. Schneider, J. Synchr. Rad. (2000), submitted.
[15] S. Shapiro, J. Axe, G. Shirane, and T. Riste, Phys. Rev. B **6**, 4332 (1972).
[16] H. Scheel, J. Bednorz, and P. Dill, Ferroelectrics **13**, 507 (1976).
[17] J.R. MacDonald, *"Impedance spectroscopy"*, (John Wiley & Sons, New York, 1987)
[18] I. Denk, W. Münch, and J. Maier, J. Am. Ceram. Soc. **78**, 3265 (1995).
[19] J. Fleig, F. Noll, and J. Maier, Ber. Bunsenges. Phys. Chem. **100**, 607 (1996).
[20] W. Zachariasen, *"Theory of X-ray diffraction in crystals"* (Wiley, New York, 1945).
[21] B. Batterman and H. Cole, Rev. Mod. Phys. **36**, 681 (1964).
[22] J. Schneider, J.-E. Jørgensen, and G. Shirane, Phase Trans. **8**, 17 (1986).
[23] J. Als-Nielsen, in *"Topics in current physics: Structure and dynamics of surfaces"*, edited by W. Schommers and P. v.Blanckenhagen (Springer, 1986), Vol. **2**.
[24] R. Cowley, Adv. Phys. **29**, 1 (1980).
[25] D. Bäuerle and W. Rehwald, Sol.State Com. **27**, 1343 (1978).
[26] J. Hastings, S. Shapiro, and B. Frazer, Phys. Rev. Lett. **40**, 237 (1978).
[27] W. Zhong and D. Vanderbilt, Phys. Rev. B **53**, 5047 (1996).
[28] M. Fisher, J. Math. Phys. **5**, 944 (1964).
[29] F. Schwabl and U. Täuber, Phys. Rev. B **43**, 11112 (1991).
[30] K. Hirota *et al.*, Phys. Rev. B. **52**, 13195 (1995).
[31] U. Rütt, H.-B. Neumann, H. Poulsen, and J. Schneider, J. Appl. Cryst. **28**, 729 (1995).
[32] H.-B. Neumann *et al.*, J. Appl. Cryst. **27**, 1030 (1994).

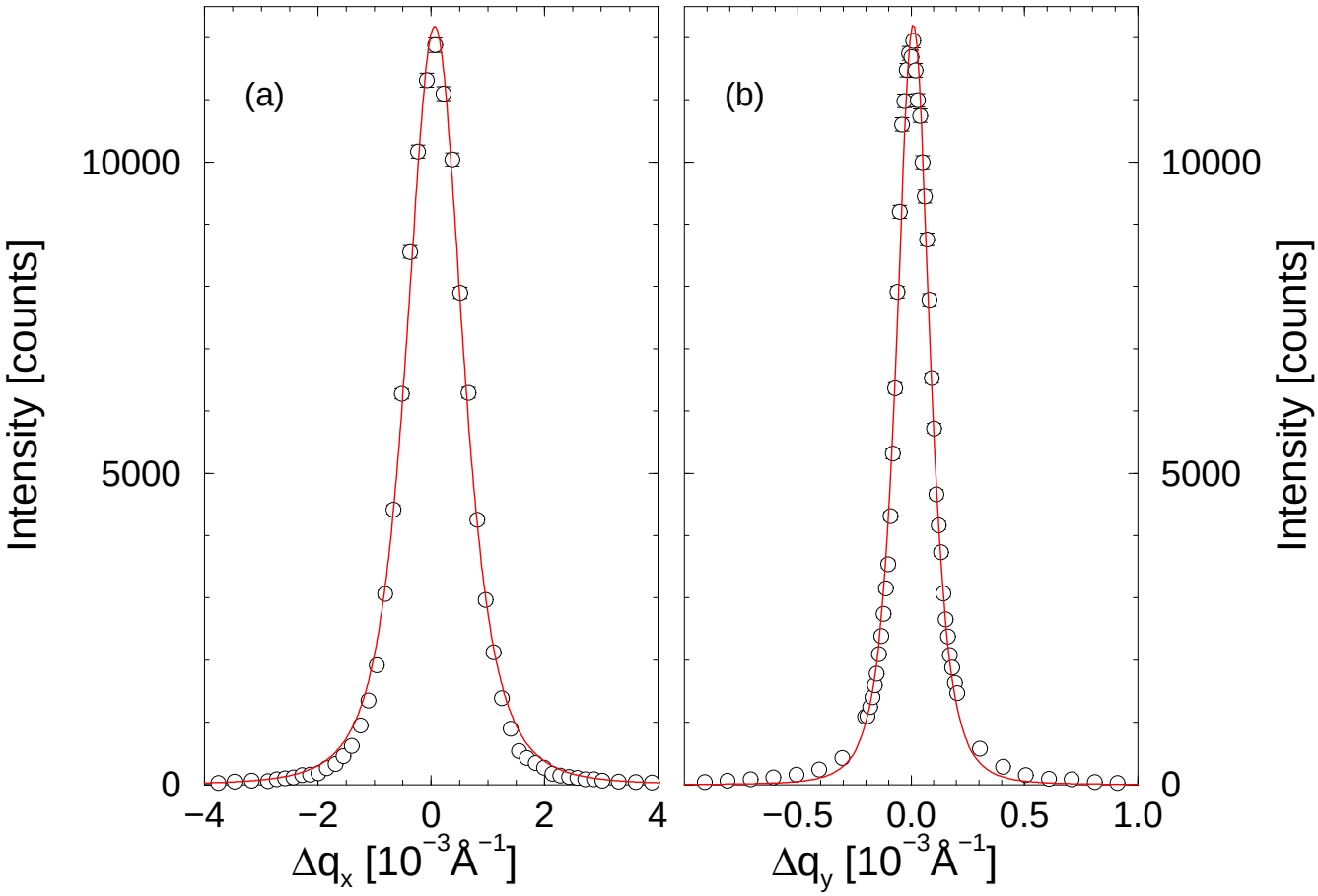

FIG. 1. Longitudinal (a) and transverse (b) scattering profiles of the (511)/2-superlattice reflection a few degrees below the critical temperature. The solid lines represent the best fits to the data using a Lorentzian-squared profile.

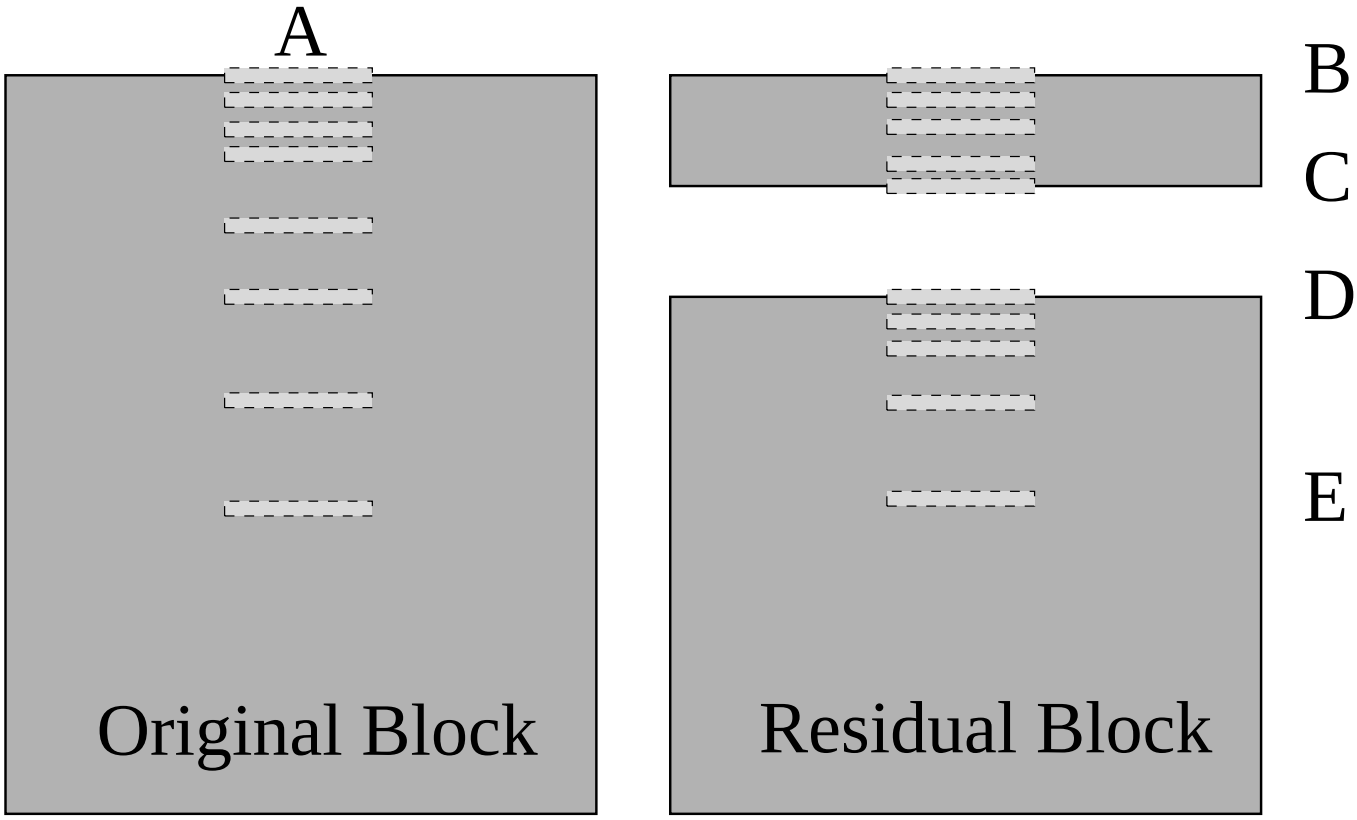

FIG. 2. Schematic drawing of the floatzone grown sample. The left hand side shows the original sample investigated in [Rue97], the right hand side shows the two samples obtained after cutting a 560 μm thick platelet from the top of the original sample. The capital letters A-E define the nomenclature for this paper. Region A corresponds to the surface of the original block. Region B and C correspond to the two surfaces of the platelet, region D denotes the surface of the residual block and region E labels the bulk of this block. The lighter rectangles (not to scale) indicate locations of the incident beam with respect to the sample surface.

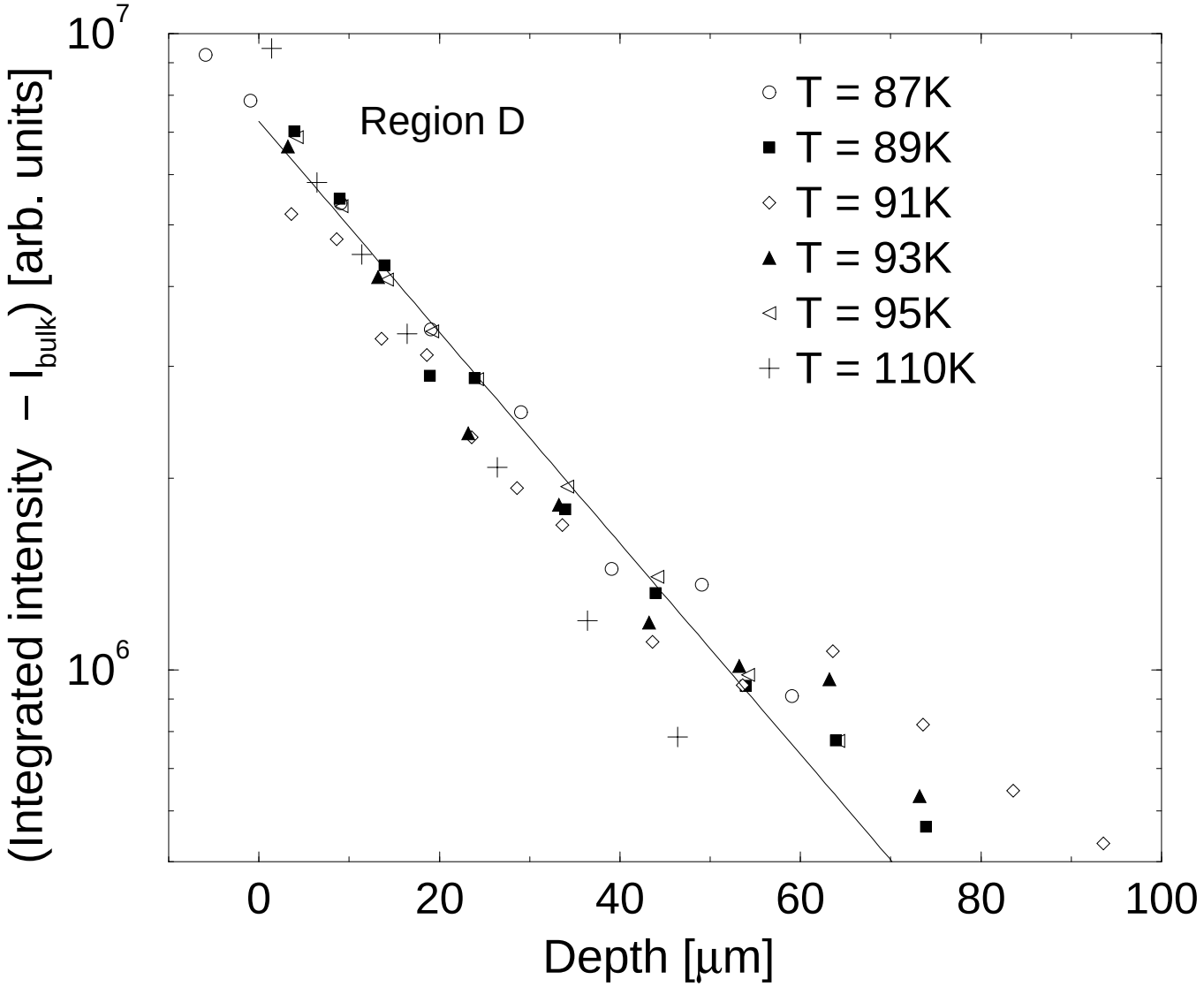

FIG. 3. Depth dependence of the integrated intensity of the (511)-reflection in region D for different temperatures around the critical temperature with respect to the corresponding bulk value I_{bulk}. The increase of the integrated intensity in the surface near region is well described by an exponential relation with a $1/e$-length of $\zeta = 26(1)\,\mu$m.

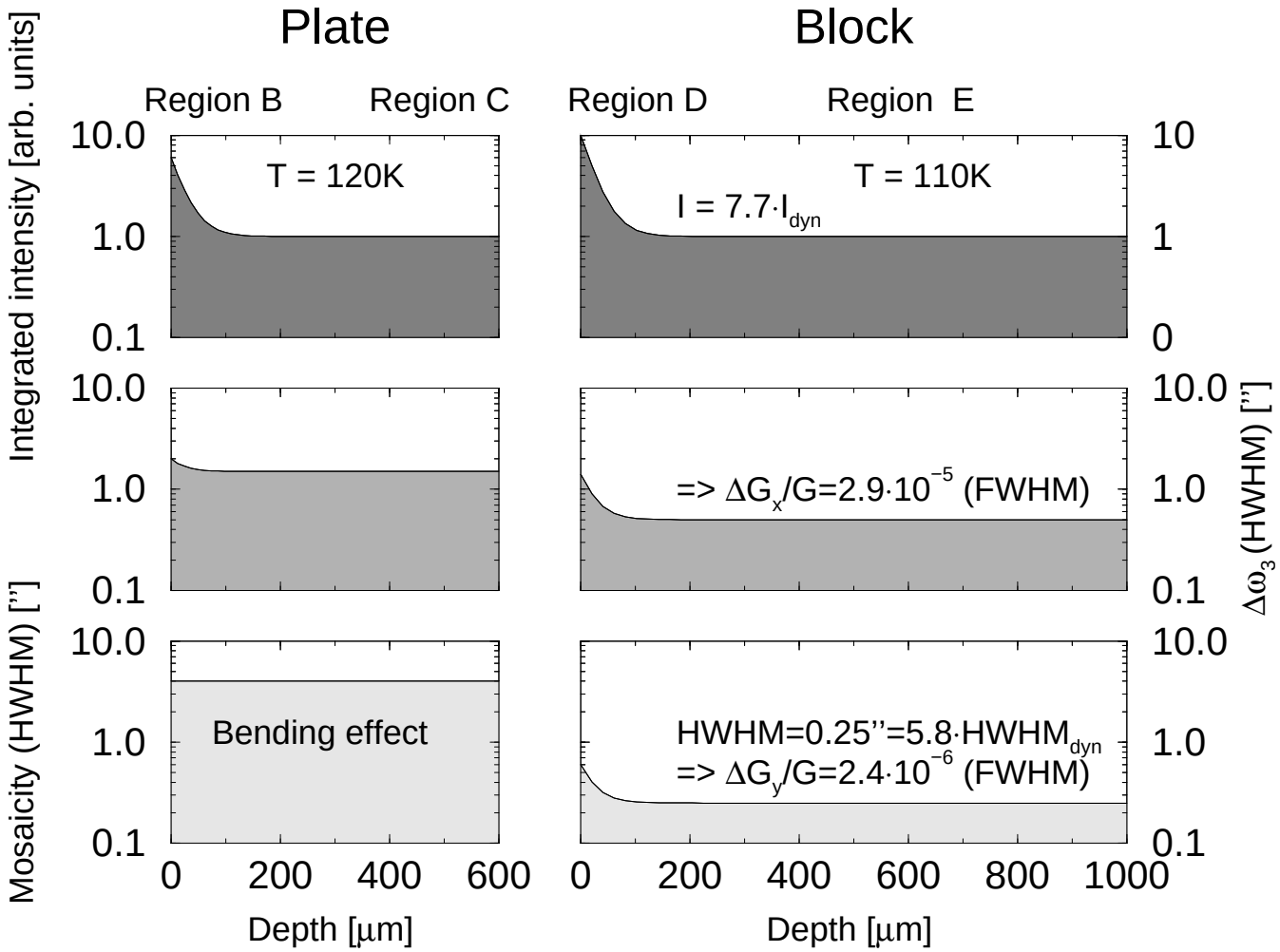

FIG. 4. Schematic view of the depth dependence of integrated intensity and the widths (HWHM) of longitudinal and transverse scans at the (511) reflection position. The surface of the residual block (D) and the old surface of the plate (B) exhibit the same features, whereas the new surface of the plate (C) shows no effects in the crystallographic quantities. The intrinsic mosaicity of the plate (picture in the lower left corner) could not be measured due to the bending of the plate. The decay of the crystallographic parameters at the different surfaces is well described by exponential functions with the same $1/e$-length $\zeta \approx 25.5(15)\ \mu$m.

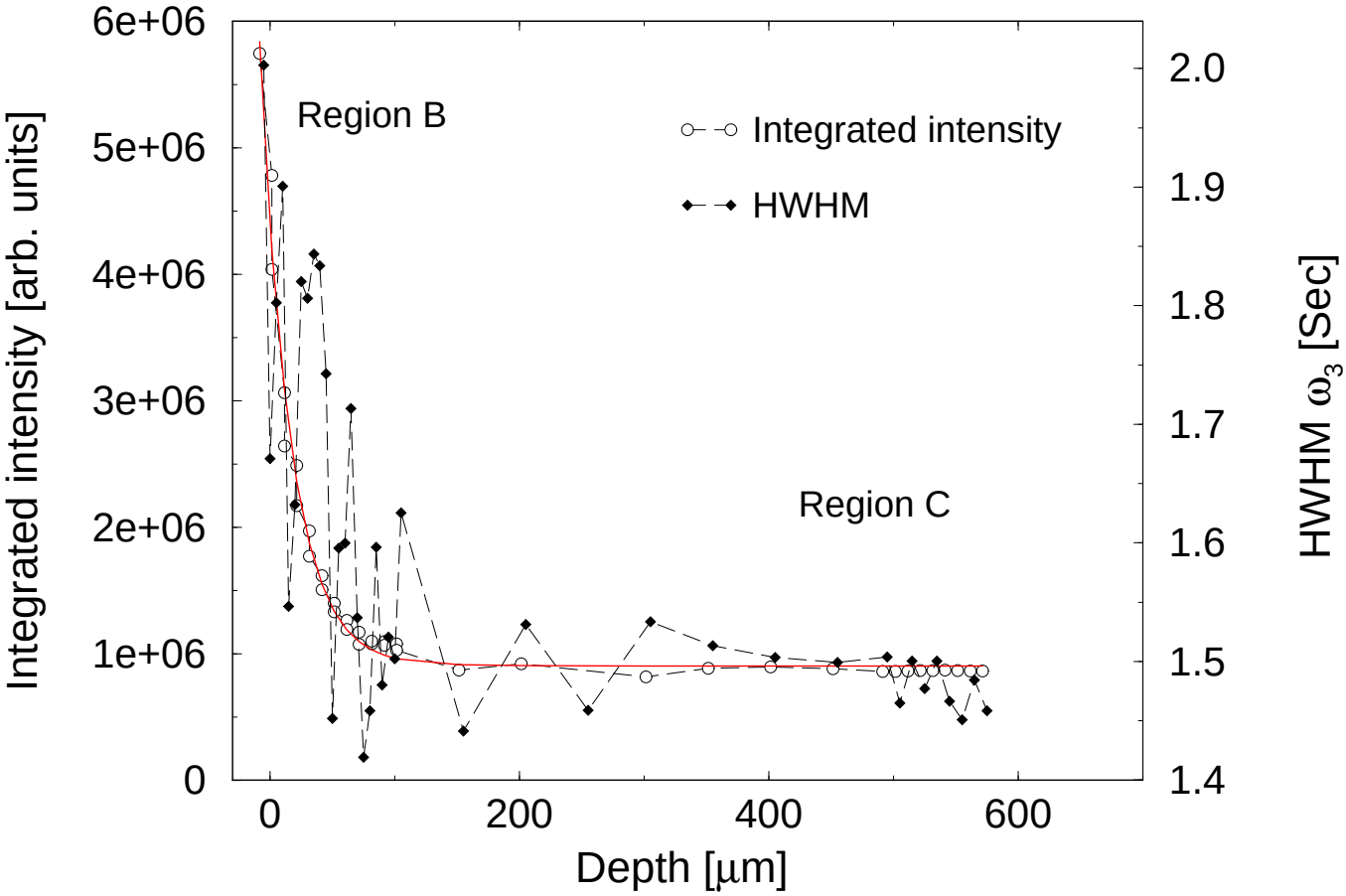

FIG. 5. Depth dependence of the integrated intensity and the HWHM of the longitudinal scans at the (511)-reflection position in the plate. The width of the longitudinal scans is proportional to the lattice parameter variations: $\Delta d/d = \frac{1}{2} \cdot \cot\theta_B \cdot \Delta\omega_3$. The left hand side corresponds to region B, an exponential increase ($(I - I_{bulk}) \propto \exp(-z\zeta)$) of both quantities is clearly visible. The $1/e$-length results to $\zeta = 25(1)\,\mu$m. On the right hand side (region C) no changes at all can be observed.

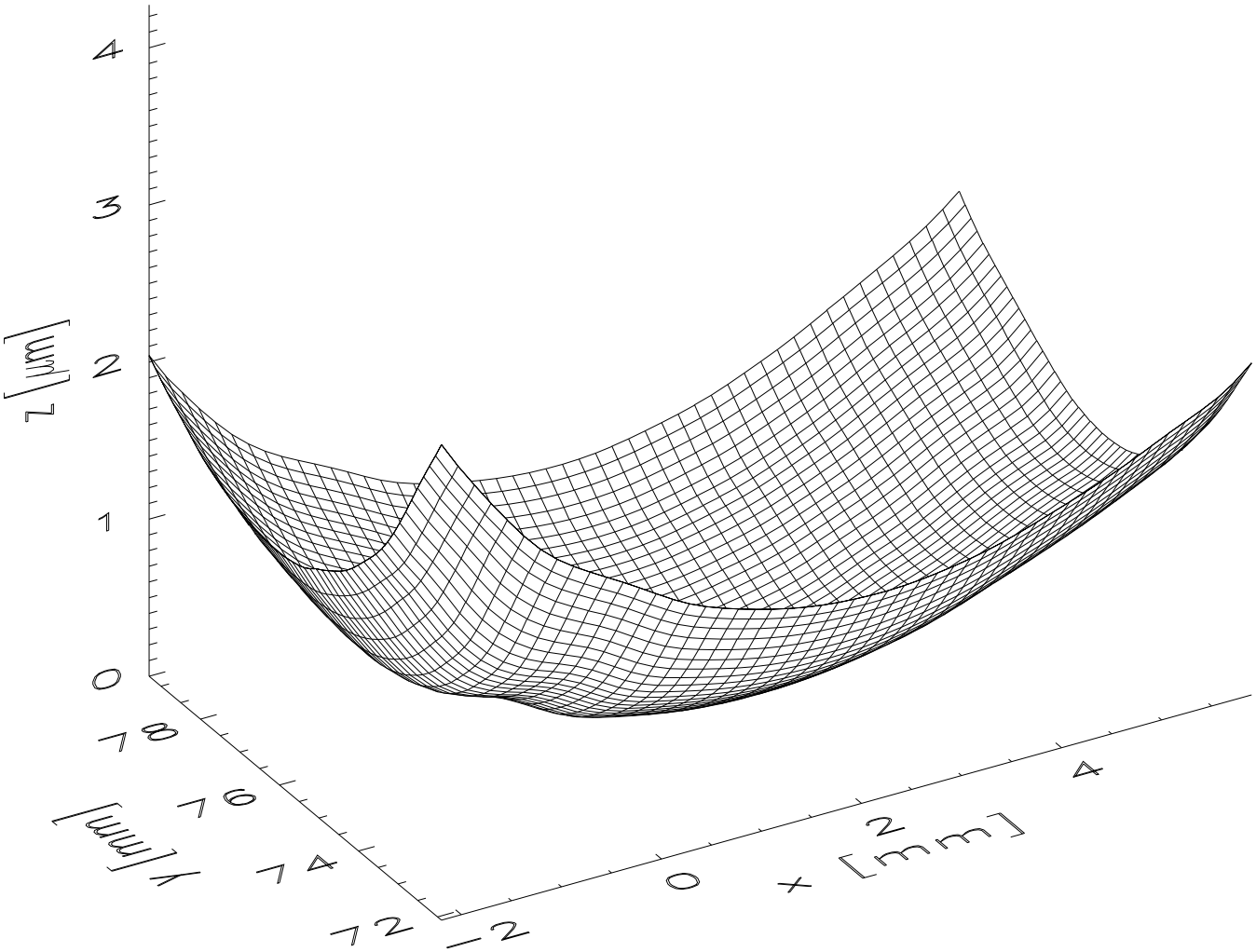

FIG. 6. Illustration of the bent plate in real-space. The bending radius is about 14 m. The upper part corresponds to region C, the lower part represents region B.

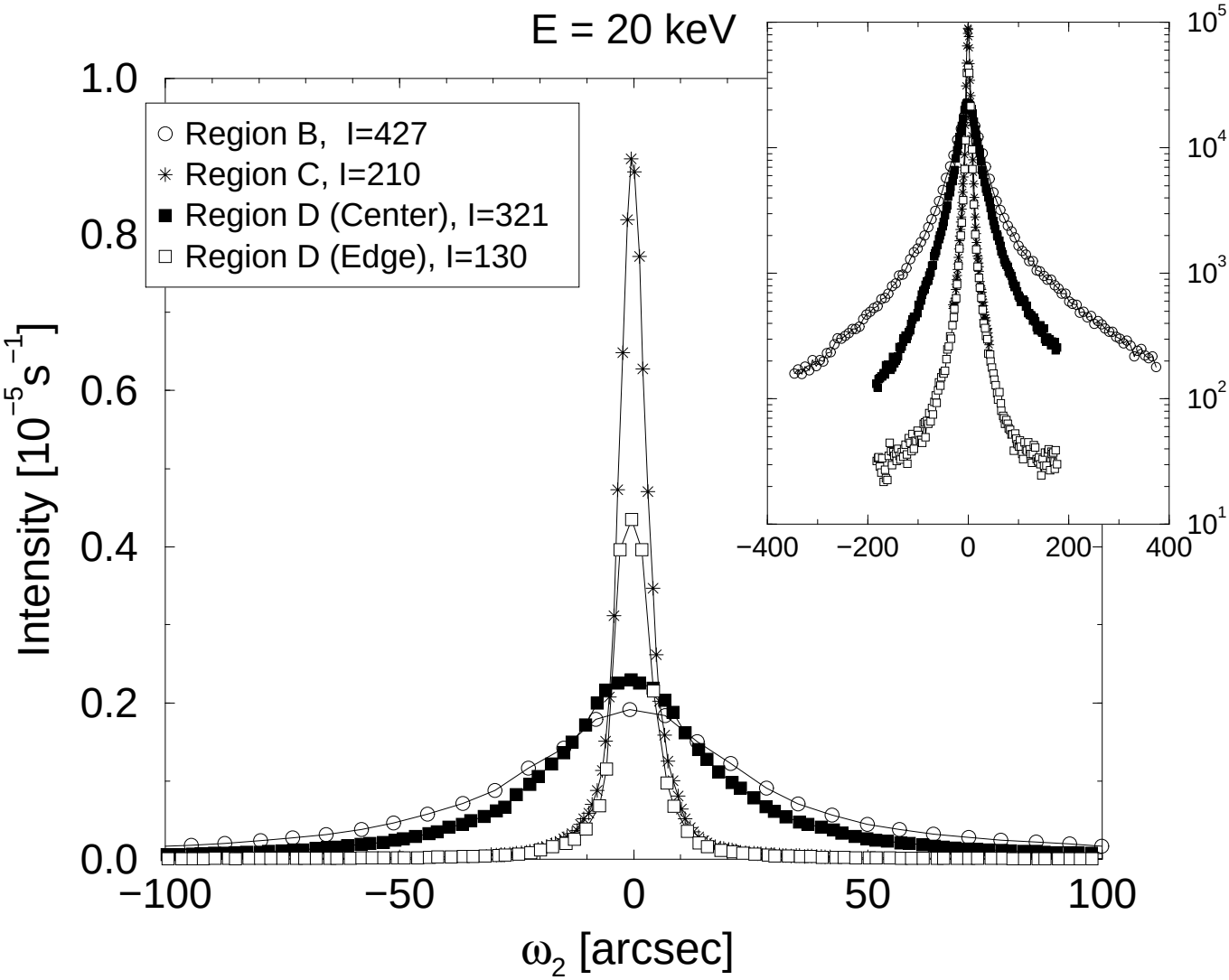

FIG. 7. Rocking curves of the (200) bragg reflection at the different surfaces of the floatzone grown-samples, measured at room temperature with 20 keV x-rays at beamline D4. The Rocking curves in region B and D are much broader than those of region C and of the edge region of the residual block. The inset shows the same data in a logarithmic scale. $I = \ldots$ represent the values of the integrated intensities of the respective scans.

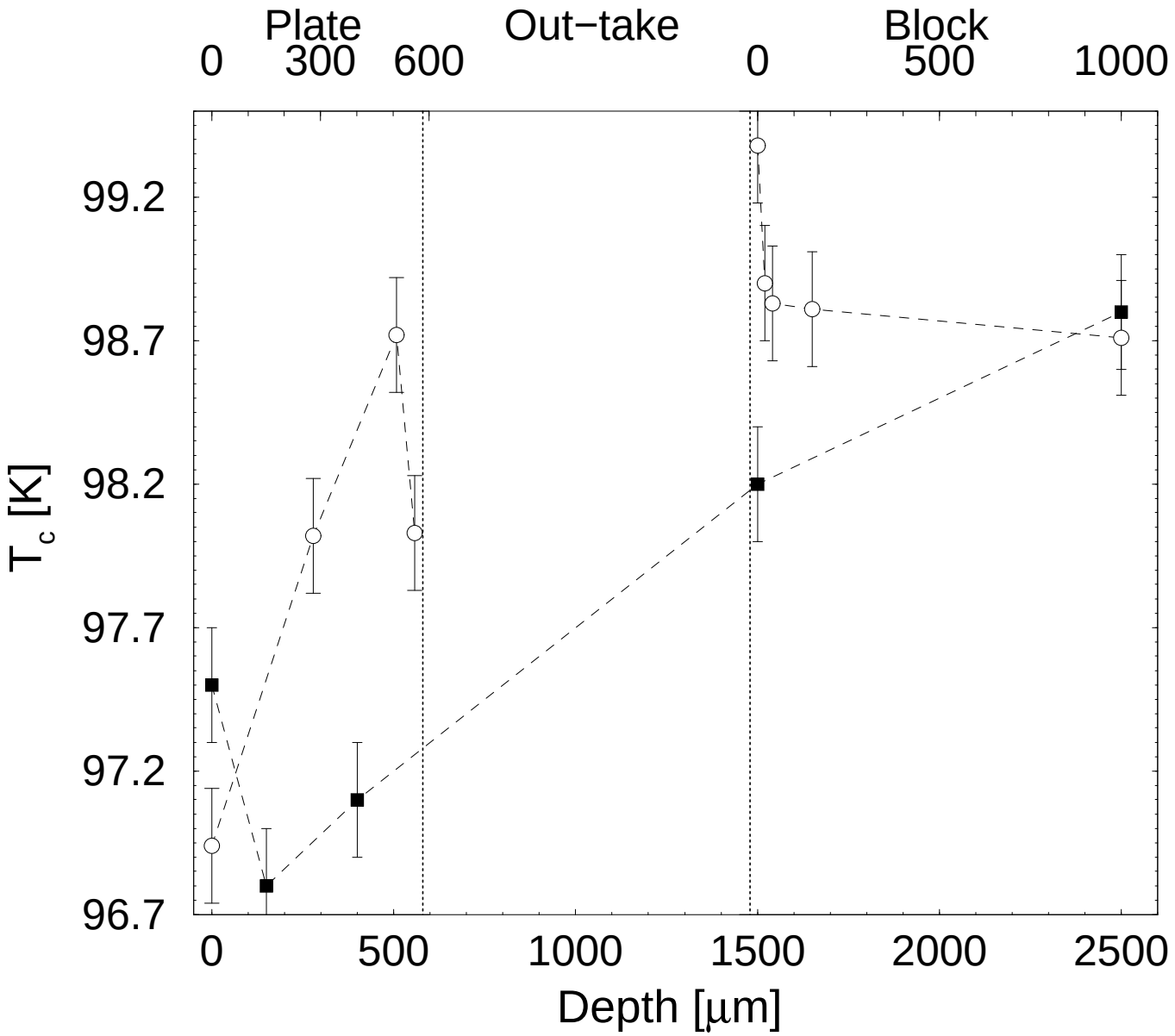

FIG. 8. Depth dependence of the critical temperatures in sample I after the cut (opaque circles), compared to the values for the original sample (black squares).

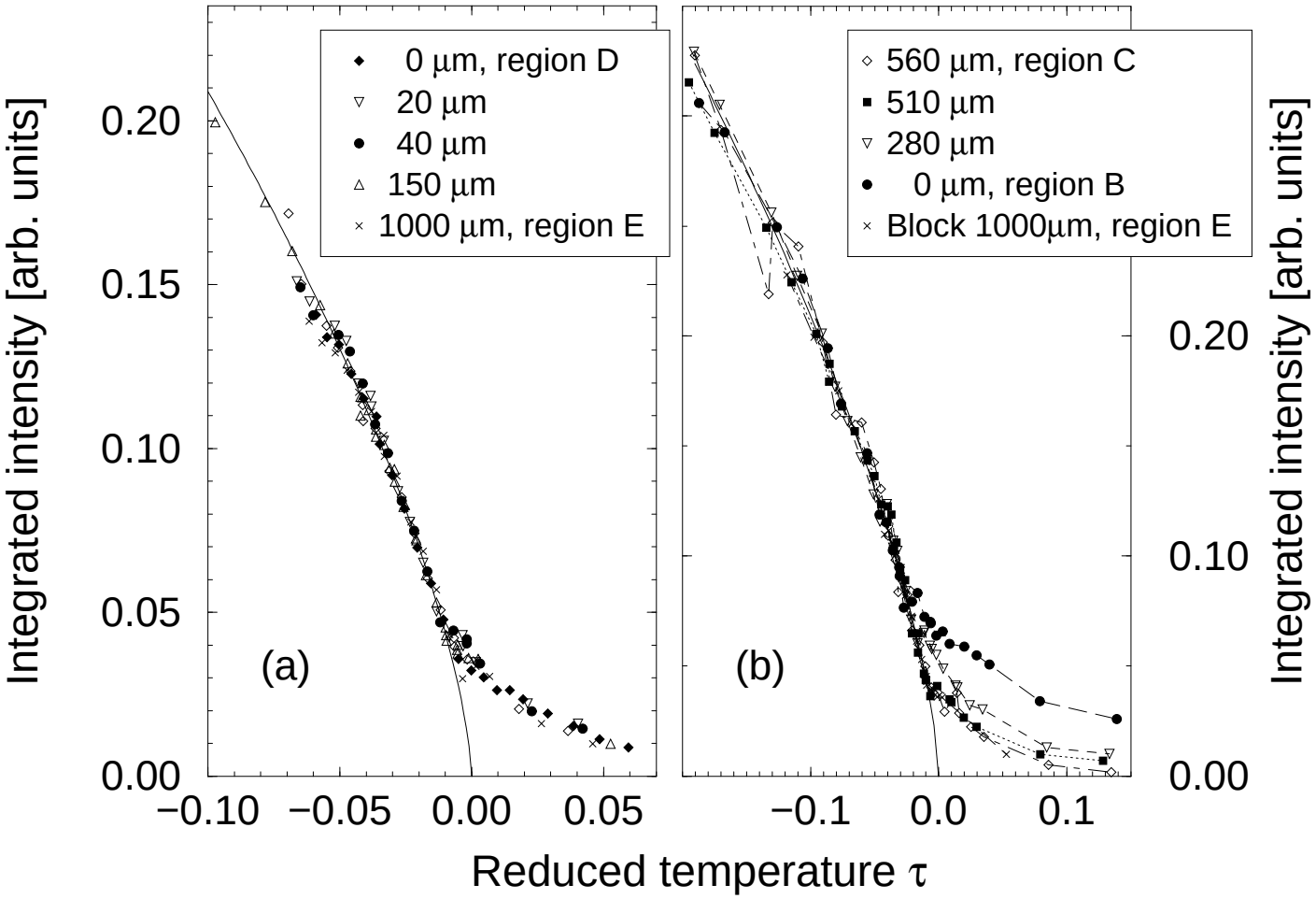

FIG. 9. Temperature dependence of the integrated intensities of the (511)/2 superlattice reflection, normalized to the respective extrapolated value at zero temperature, for different positions (a) in the residual block and (b) the plate. The tail above T_c is almost independent of the distance from the surface. Only in region B significant changes in the temperature dependence of the tail are observed.

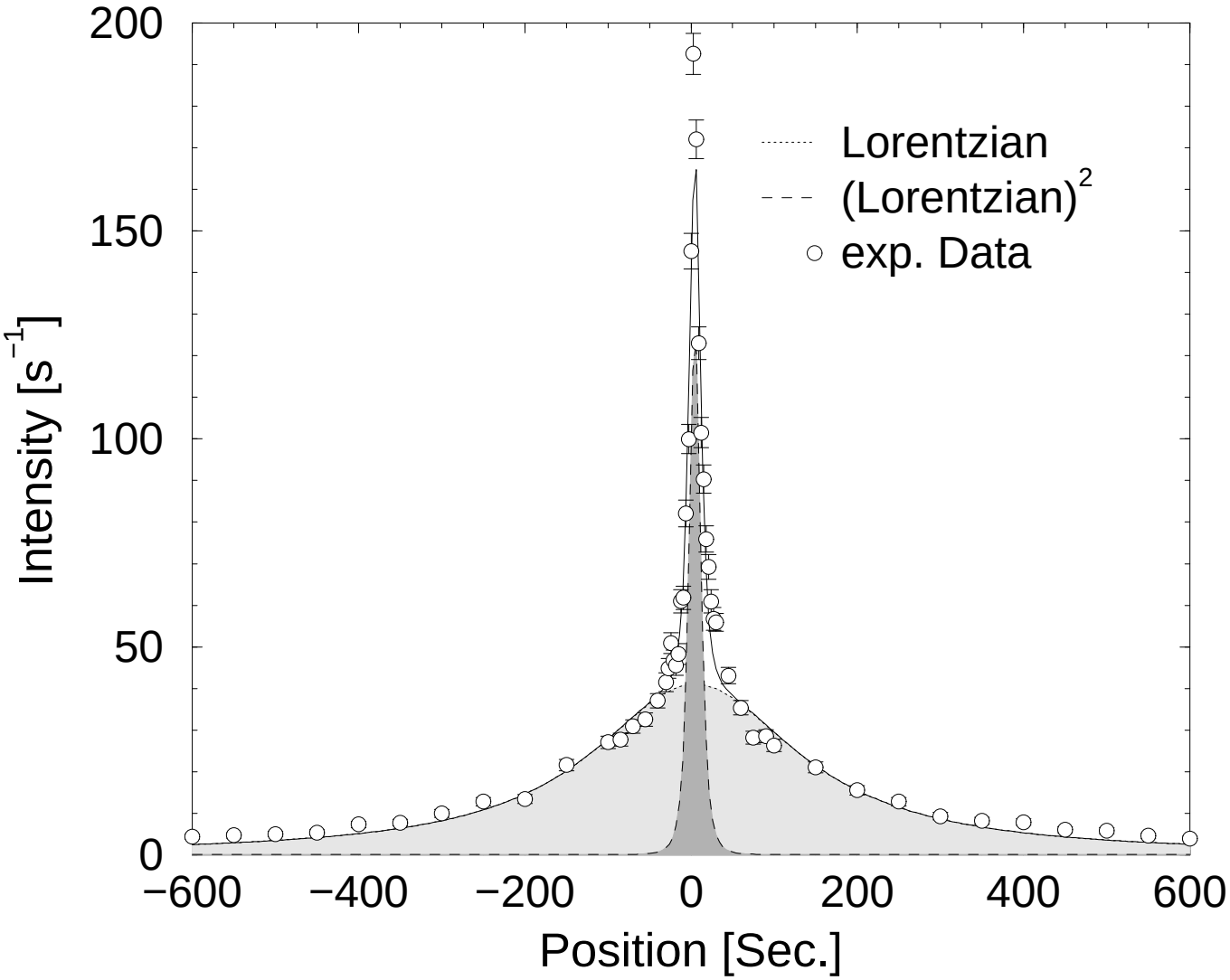

FIG. 10. Transverse scan 0.5 K above T_c in a distance of 20 μm from the surface of the residual block (region D). Additional to the broad Lorentzian distribution a sharp Lorentzian squared profile is visible at the position of the superlattice reflection.

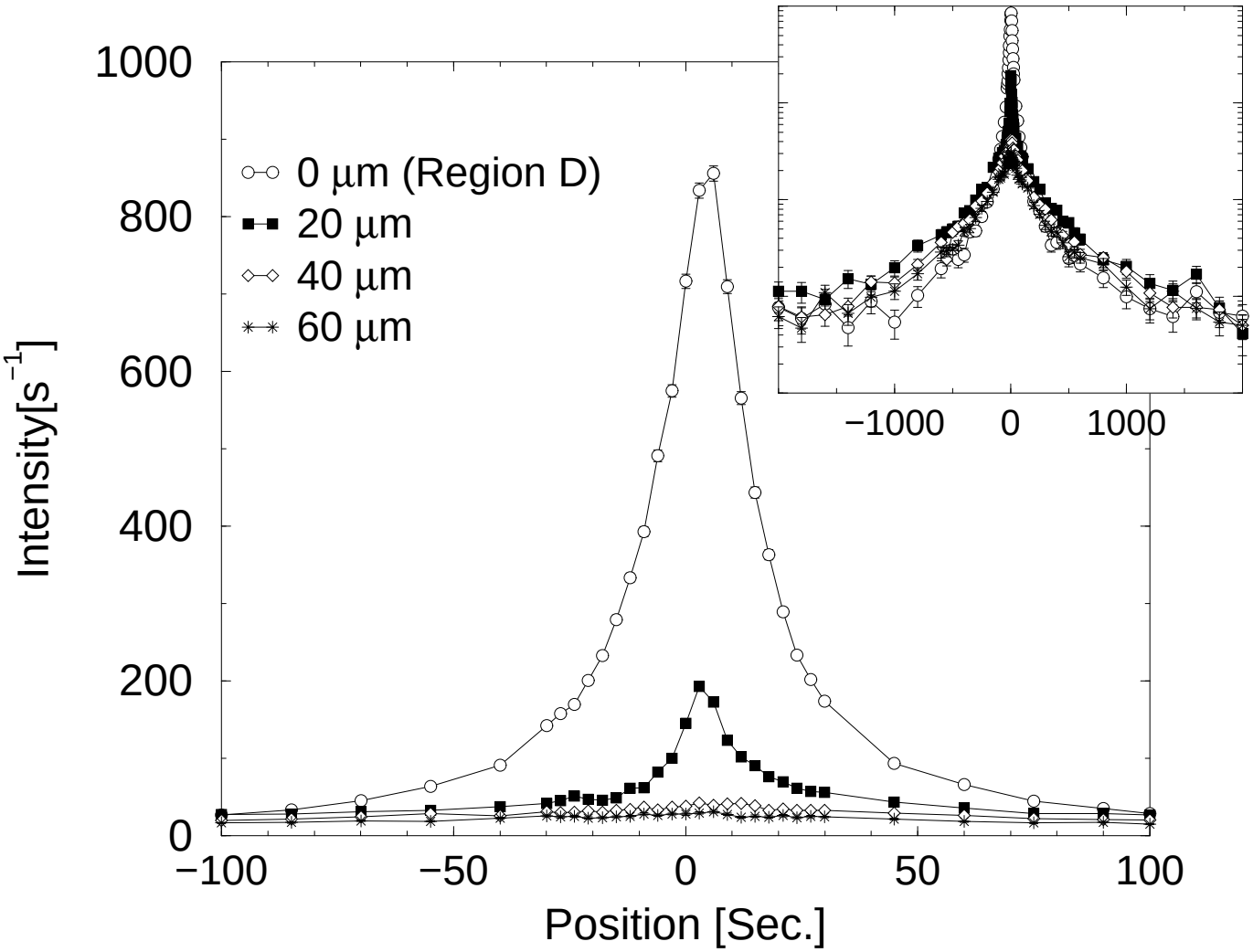

FIG. 11. Transverse scan profile of the (511)/2 superlattice reflection about 1 K above the critical temperature for different distances to the surface of the residual floatzone grown-block (sample I, region D). For the top 20 μm the intensity is strongly enhanced in a narrow region around the superlattice position. The inset shows the measured data over a much larger angular range in a logarithmic scale. It can be seen that without considering the sharp component all profiles are almost identical.

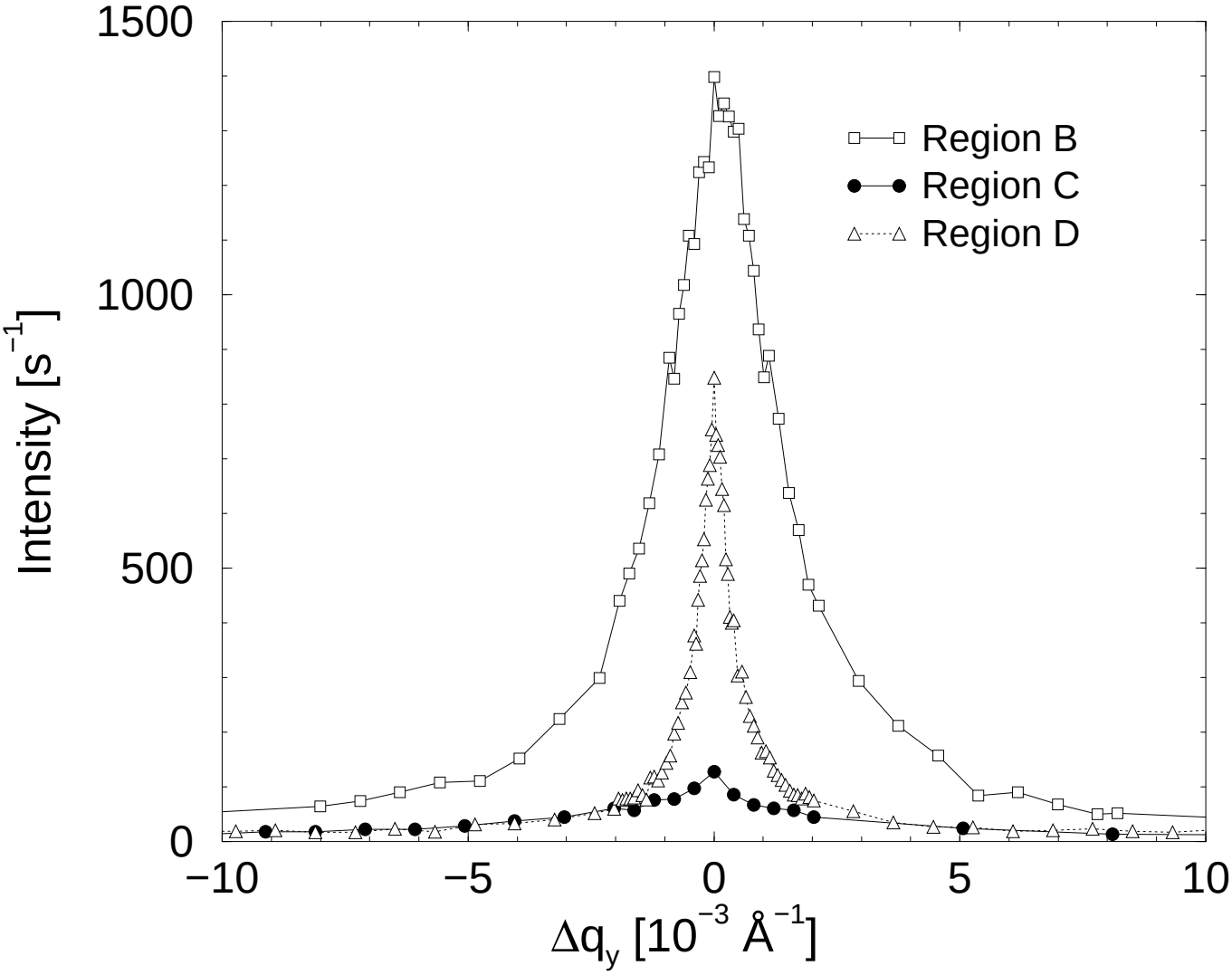

FIG. 12. Comparison of the scattering profiles of the (511)/2 superlattice reflections of sample I 1 K above T_c measured close to the three different surfaces. The old surface of the plate (region B) differs strongly from the other ones, whereas the new surface of the plate (region C) and the residual block (region D) differ only in the narrow region in the center of the plot. The broad component is identical for the latter two surfaces, but at the residual block the sharp component can be observed additionally.

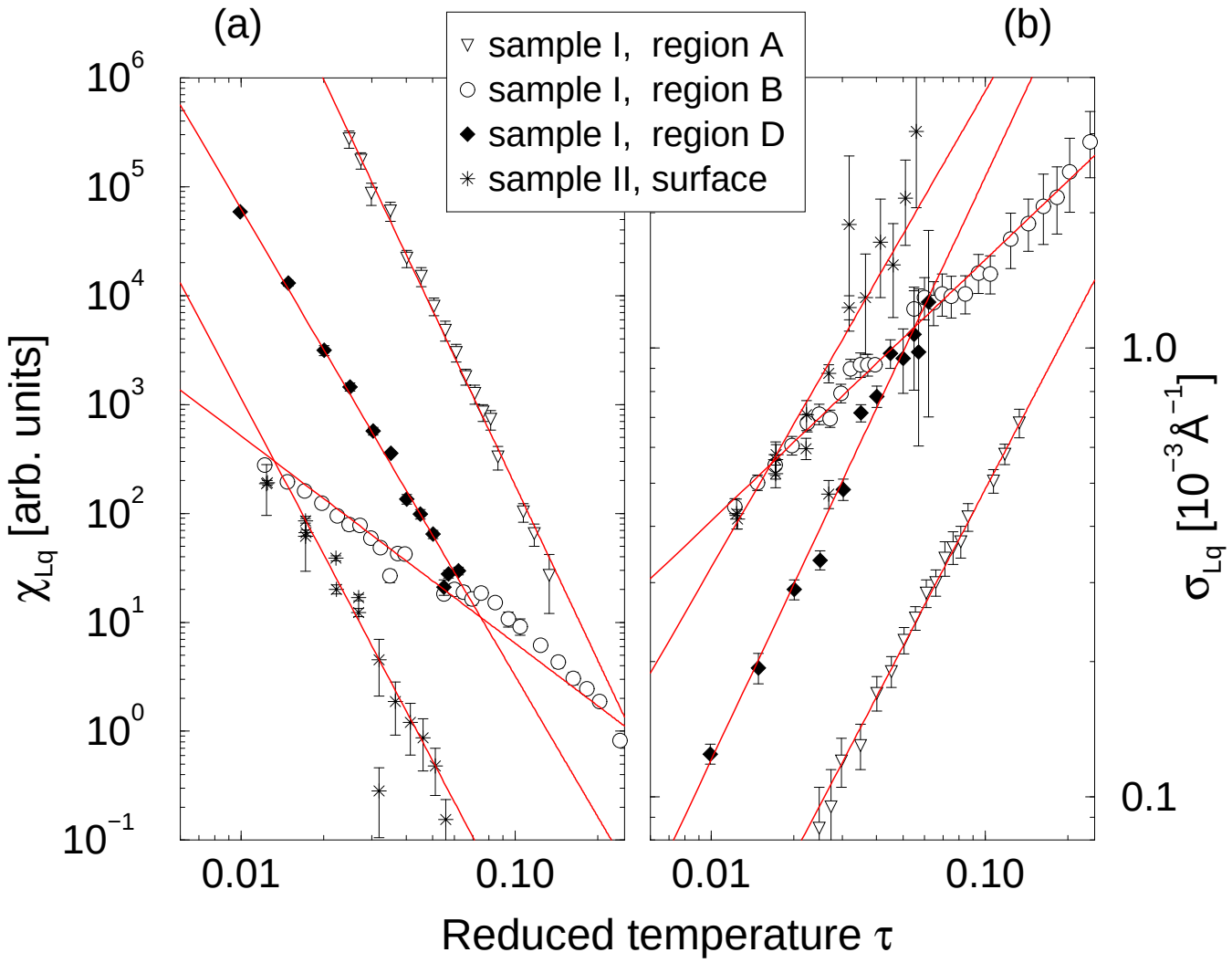

FIG. 13. Temperature dependence (a) of the inverse correlation length σ_{Lq} and (b) of the susceptibility χ_{Lq} of the sharp component for the different surfaces. The critical exponents ν_s and γ_s are similar for most of the investigated surfaces, but they strongly deviate at the old surface of the plate (region C).

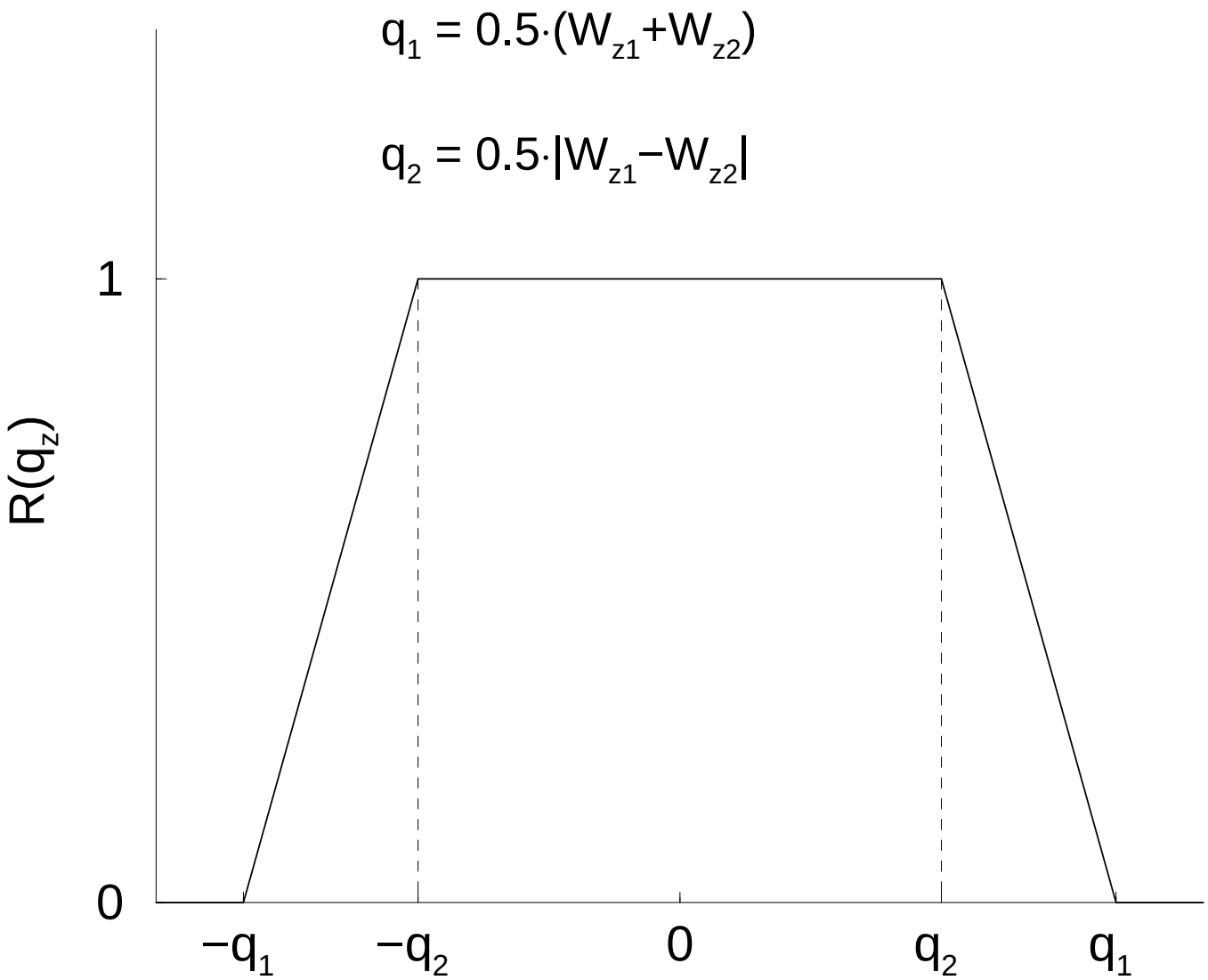

FIG. 14. Resolution function perpendicular to the scattering plane. The horizontal part of the trapezoid has a width of $2q_2 = |W_{z1} - W_{z2}|$, the width of the sloped parts just corresponds to the width of the smaller slit. In the case $W_{z1} \ll W_{z2}$ the trapezoid degenerates to a rectangle.

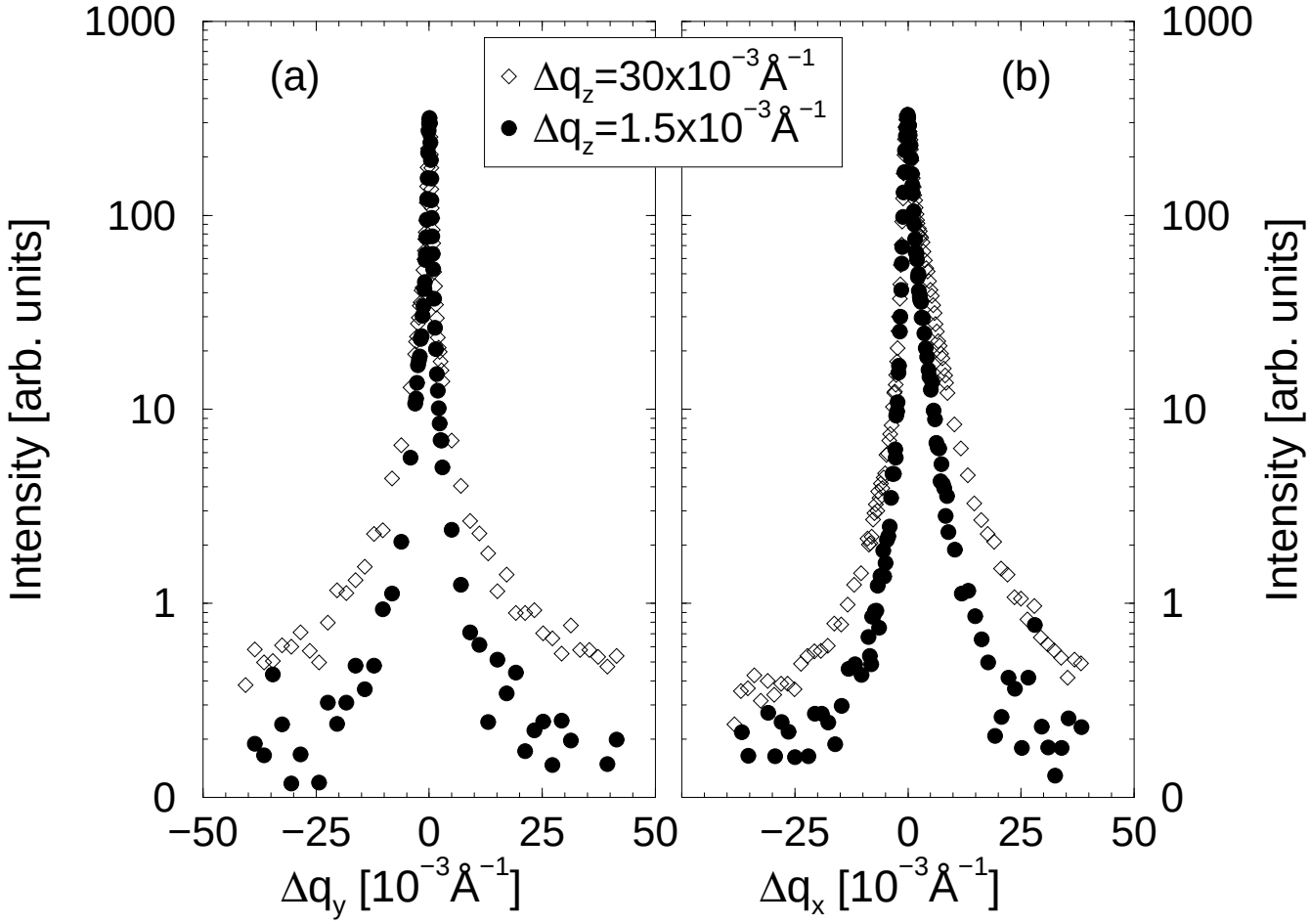

FIG. 15. Suppression of the broad component due to improvement of the resolution vertical to the scattering plane shown for transverse (a) and longitudinal (b) scans. Filled circles refer to scans with $\Delta q_z = 1.5\times10^{-3}$ Å^{-1}, open diamonds represent scans with $\Delta q_z = 30\times10^{-3}$ Å^{-1}.

Sample #	Growth method	n_O [cm^{-3}]	T_c [K]
I	Float-zone grown	$6.1(2) \times 10^{18}$	98.8(2)
II	Flux grown	$2.8(2) \times 10^{18}$	102.6(2)
III	Verneuil (oxidised)	$7.4(2) \times 10^{16}$	105.7(2)
IV	Verneuil (as grown)	$7.6(2) \times 10^{16}$	105.8(2)
V	Verneuil (reduced)	$1.7(1) \times 10^{19}$	101.0(2)

TABLE I. Nomenclature of the different samples, concentrations of oxygen vacancies and critical temperatures.

sample #	Broad component			
	ν_b	γ_b	γ_b/ν_b	$\beta = (3\nu_b - \gamma_b)/2$
Original block				
I, region E	1.07(6)	2.9(2)	**2.71(24)**	0.16(13)
I, region A	1.02(4)	2.32(7)	**2.27 (11)**	0.37(7)
Residual plate				
I, region B	1.19	2.23(10)	**1.87(11)**	0.67(8)
I, region C	1.19	2.83(10)	**2.38(13)**	0.37(8)
Residual block				
I, region D	1.19	2.53(3)	**2.13(9)**	0.52(6)
I, region E	1.19(4)	2.89(4)	**2.43(9)**	0.34(6)
II	0.9(1)	1.7(1)	**1.9(2)**	0.50(16)
III	0.73(7)	1.49(15)	**2.04(28)**	0.35(13)
IV	0.79(2)	1.58(7)	**2.00(10)**	0.40(5)
V	1.18(3)	2.45(7)	**2.08(8)**	0.55(6)

TABLE II. Critical exponents ν_b and γ_b for the broad component. Due to the scaling relations the ratio γ_b/ν_b should be close to 2.0. Also, $\beta = (3\nu_b - \gamma_b)/2$ is calculable using the scaling relations.

sample #	Sharp component		
	ν_s	γ_s	γ_s/ν_s
I, region A	1.17(4)	5.33(9)	**4.6(2)**
I, region B	0.58(5)	1.9(2)	**3.3(4)**
I, region D	1.30(5)	4.29(10)	**3.30(14)**
II	1.1(1)	4.8(1)	**4.4(4)**

TABLE III. Critical exponents ν_s and γ_s as well as the ratio γ_s/ν_s for the sharp component. The ratio γ_s/ν_s is more likely close to 4 than to the expected value of 2.